TU Delft

Delft University of Technology

Aerodynamic Performance of a Wingtip-Mounted Tractor Propeller Configuration in Windmilling and Energy-Harvesting Conditions

Sinnige, Tomas; Stokkermans, Tom; van Arnhem, Nando; Veldhuis, Leo

DOI
10.2514/6.2019-3033

Publication date
2019

Document Version
Final published version

Published in
AIAA Aviation 2019 Forum

Citation (APA)
Sinnige, T., Stokkermans, T., van Arnhem, N., & Veldhuis, L. (2019). Aerodynamic Performance of a Wingtip-Mounted Tractor Propeller Configuration in Windmilling and Energy-Harvesting Conditions. In *AIAA Aviation 2019 Forum* (pp. 1-17). Article AIAA-2019-3033 (AIAA Aviation 2019 Forum). American Institute of Aeronautics and Astronautics Inc. (AIAA). https://doi.org/10.2514/6.2019-3033

Important note
To cite this publication, please use the final published version (if applicable).
Please check the document version above.

Copyright
Other than for strictly personal use, it is not permitted to download, forward or distribute the text or part of it, without the consent of the author(s) and/or copyright holder(s), unless the work is under an open content license such as Creative Commons.

Takedown policy
Please contact us and provide details if you believe this document breaches copyrights.
We will remove access to the work immediately and investigate your claim.

This work is downloaded from Delft University of Technology.
For technical reasons the number of authors shown on this cover page is limited to a maximum of 10.

© 2019 by T. Sinnige, T. C. A. Stokkermans, N. van Arnhem, and L. L. M. Veldhuis.
https://doi.org/10.2514/6.2019-3033

Aerodynamic Performance of a Wingtip-Mounted Tractor Propeller Configuration in Windmilling and Energy-Harvesting Conditions

Tomas Sinnige*, Tom C. A. Stokkermans†, Nando van Arnhem‡, and Leo L. M. Veldhuis§
Delft University of Technology, 2629 HS, Delft, The Netherlands

Wingtip-mounted tractor propellers enhance aerodynamic performance by attenuating the wingtip vortex with the propeller slipstream and inducing a favorable upwash on the wing. However, the close coupling between propeller and wing means that wing performance may be degraded when the propeller produces negative thrust. This paper analyzes the aerodynamic interaction effects due to the wingtip-mounted propeller under such conditions, that occur when the propeller is windmilling or used for energy harvesting. Experiments in a low-speed wind tunnel and simulations with a RANS solver highlighted the drop in wing performance at negative thrust for the case with inboard-up rotation. The interaction phenomena are reversed compared to the beneficial propulsive case, since the inflow velocity and angle of attack are now reduced on the part of the wing washed by the slipstream. Because of the reversal of the swirl in the slipstream at negative thrust, the interaction is then favorable with outboard-up rotation. For the considered propeller, that was not optimized for operation at negative thrust, the energy-harvesting efficiency was about 10%. This can be improved for future designs by optimizing the blade geometry and pitch setting of the propeller.

Nomenclature

A_{ref}	=	reference area used in Eq. 3
C_D	=	$D/q_\infty S$, drag coefficient
C_{f}	=	τ_{w}/q_∞, skin-friction coefficient
C_L	=	$L/q_\infty S$, lift coefficient
C_P	=	$P/\rho_\infty n^3 D^5$, propeller power coefficient
C_p	=	$(p - p_\infty)/q_\infty$, pressure coefficient
C_T	=	$T/\rho_\infty n^2 D^4$, propeller thrust coefficient
c	=	chord length, m
c_d, c_l	=	section drag, lift coefficient
c_q, c_t	=	section torque, thrust coefficient
c_P	=	$P'/\rho_\infty n^3 D^4$, section power coefficient
c_T	=	$T'/\rho_\infty n^2 D^3$, section thrust coefficient
D	=	propeller diameter, m; drag force, N
J	=	V_∞/nD, propeller advance ratio
L	=	lift force, N
n	=	propeller rotational speed, Hz
P	=	propeller power, W
P_{C}	=	$P/\rho_\infty V_\infty^3 D^2$, propeller power coefficient based on freestream dynamic pressure
p	=	static pressure, Pa
q	=	$\rho V^2/2$, dynamic pressure, Pa
R	=	propeller radius, m
R_{nac}	=	nacelle radius, m
Re	=	Reynolds number
r	=	radial coordinate, m
S	=	cs, wing reference area, m^2
s	=	span (including nacelle), m
s_{w}	=	wing span (excluding nacelle), m
T	=	propeller thrust, N
T_{C}	=	$T/q_\infty D^2$, propeller thrust coefficient based on freestream dynamic pressure
V	=	velocity, m/s
V_{eff}	=	effective velocity at blade section, m/s
X, Y, Z	=	axial, spanwise, vertical coordinate from propeller center, m
x	=	axial coordinate from wing leading edge, m
y	=	spanwise coordinate from wing root, m
y^+	=	dimensionless wall distance
α	=	angle of attack, deg
β	=	blade pitch angle at 75% of the radius, deg
η_{eh}	=	$P/\frac{1}{2}\rho_\infty \pi R^2 V_\infty^3$, energy-harvesting efficiency
θ	=	swirl angle, deg
ρ	=	air density, kg/m^3
τ_{w}	=	wall shear stress, Pa
ϕ	=	propeller circumferential coordinate, rad

*Assistant professor, Flight Performance and Propulsion Section, Faculty of Aerospace Engineering, Kluyverweg 1; T.Sinnige@tudelft.nl. Member AIAA.
†PhD Candidate, Flight Performance and Propulsion Section, Faculty of Aerospace Engineering, Kluyverweg 1. Member AIAA.
‡PhD Candidate, Flight Performance and Propulsion Section, Faculty of Aerospace Engineering, Kluyverweg 1. Member AIAA.
§Full professor, Flight Performance and Propulsion Section, Faculty of Aerospace Engineering, Kluyverweg 1. Member AIAA.

© 2019 by T. Sinnige, T. C. A. Stokkermans, N. van Arnhem, and L. L. M. Veldhuis.
https://doi.org/10.2514/6.2019-3033

Sub- and superscripts

a	=	axial	t	=	tangential
dwns	=	in downstream survey plane	ups	=	in upstream survey plane
IU	=	inboard-up propeller-rotation case	∞	=	freestream
int	=	integral	$'$	=	per unit span
OU	=	outboard-up propeller-rotation case			

I. Introduction

The need to reduce emissions of the rapidly growing air transportation sector has spurred interest in hybrid-electric and fully-electric aircraft propulsion systems. Because of the limited effect of scaling on the performance of electric motors, electrification of aircraft enables novel technologies such as distributed propulsion and tip-mounted propellers. In this way, vehicle performance can be enhanced through improved propulsion integration, which can offset one of the main disadvantages of batteries: low energy density compared to jet fuels [1]. A prime example is the tip-mounted propeller, that promises significant aerodynamic benefits due to integration synergies. A recent comprehensive experimental study by the authors [2] discussed the aerodynamic interaction effects for wingtip-mounted tractor propellers, and confirmed the potential aerodynamic benefit compared to a conventional propeller-wing layout in case of inboard-up rotation. The results complemented previous work [3, 4] and recent research related to the NASA X-57 Maxwell [5, 6]. In all studies published so far, the propeller was at positive thrust setting to simulate the propulsive case.

Besides opportunities for advanced propulsion integration, electric propulsion also enables energy harvesting. During parts of the mission for which no power input is required, the motor(s) can be used as generator(s). As a result, energy can be recovered during flight, thereby reducing the energy consumption for a given mission. One way of harvesting energy is to use one or more propellers as airborne wind turbines during parts of the mission which do not require energy input. By operating the blade sections at negative angle of attack, the direction of the forces is inverted compared to the propulsive mode. This is sketched in Fig. 1 for the case of a propeller at a given pitch angle. The negative torque corresponds to a negative power, which can be converted into electricity by the motor. This approach has been proposed before for gliders [7–10] and naval applications [11]. More recently, work by general-aviation manufacturer Pipistrel [12] confirmed the potential of energy recovery through regenerative propellers for an electric aircraft optimized for training missions. Besides potential applications to aircraft, energy-harvesting rotors are also being considered for airborne wind-energy systems, that use the rotors in propulsive mode for lift-off and hover [13].

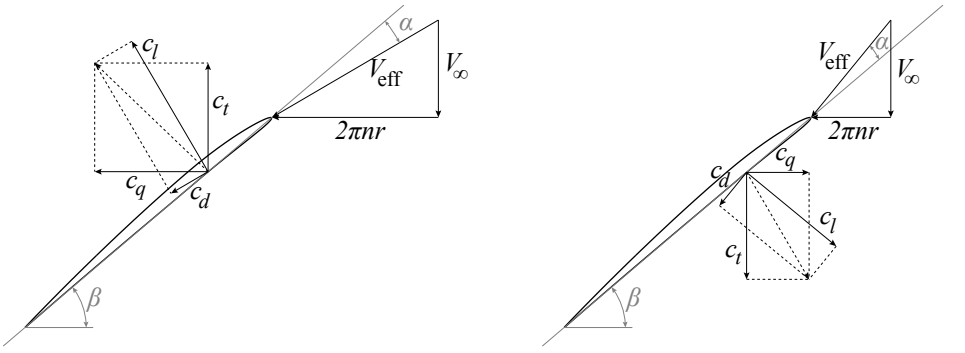

a) Propulsive mode **b) Energy-harvesting mode**

Fig. 1 Velocity triangles at a fixed-pitch propeller blade section in propulsive and energy-harvesting modes.

In contrast to the limited research focused on unducted rotors, energy harvesting in windmilling conditions has been addressed in more detail for rotors of turbofans [14–16]. Experimental, numerical, and theoretical studies confirmed the potential for power extraction in windmilling conditions, including consideration of the 'negative rotation cases' with reversed rotational direction of the rotor. During free windmilling, the rotor blade loading typically features a mixed compressor/turbine operation [15, 16], with positive loading (compressor operation) on the inboard part of the blade and negative loading (turbine operation) on the outboard part. At higher (negative) loading conditions, the whole blade is in turbine operation [15]. However, there are several differences compared to the propeller case. The presence of the casing in turbofan applications modifies the tip effects compared to the unducted propeller case. Furthermore, it causes an inlet distortion due to viscous effects [16]. Besides the direct effects on the rotor, for turbofan applications the

© 2019 by T. Sinnige, T. C. A. Stokkermans, N. van Arnhem, and L. L. M. Veldhuis.
https://doi.org/10.2514/6.2019-3033

flowfield is also affected by the stator response. During turbine operation, the stator vanes experience large negative angles of attack, which leads to stall [14]. This affects the overall mass flow rate through the engine, and will have an adverse effect on the system performance. This is not a concern for propeller applications with a single blade row.

Considering the tight integration between the propulsion system and the airframe that is typical of electric aircraft designs, the use of propellers as energy harvesters will affect the overall vehicle performance. For aircraft with wingtip-mounted tractor propellers, the performance depends strongly on the characteristics of the propeller slipstream. In propulsive mode, the enhanced dynamic pressure and swirl in the slipstream provide a performance benefit in case of inboard-up rotation [2]. If the propellers generate negative thrust, for example in an engine-inoperative condition with windmilling or feathered propellers, or in energy-harvesting mode, the slipstream will be markedly different from that when operating the propeller in the conventional propulsive mode. The lower dynamic pressure and swirl in the slipstream will cause a loss of lift on the wing, thereby adversely affecting the vehicle performance.

Previous work on tip-mounted propellers has not considered the consequence of negative propeller thrust on system performance. This paper analyzes the aerodynamic interaction effects occurring in such conditions for a wingtip-mounted tractor propeller configuration. The integral forces and wing loading are discussed based on data obtained from experiments performed in a low-speed wind tunnel. These experimental data are complemented by numerical results, that provide detailed flowfield information and loading distributions on the blades and the wing. The numerical data are also used to assess the energy-harvesting potential of the considered propeller.

II. Methods

A. Geometry

The experimental and numerical investigations considered the same propeller and wing geometries. Figure 2 provides photographs of the models used in the experiment. Technical drawings and a CAD model of the setup are available through Ref. [2] (Model 1).

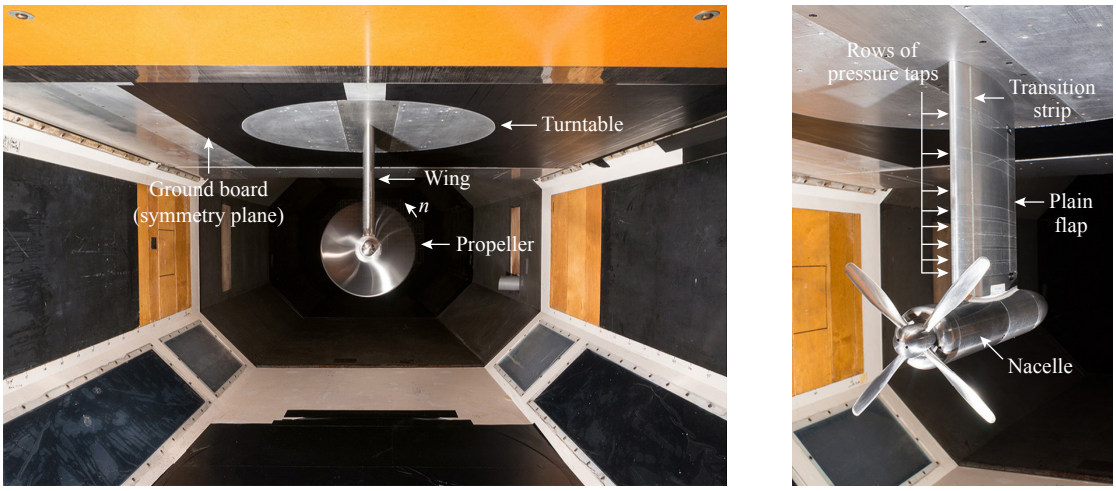

a) Front view **b) Close-up of models**

Fig. 2 Experimental setup in Delft University of Technology's Low-Turbulence Tunnel [2].

1. Propeller

The considered propeller has a diameter of 0.237 m and four blades set to a pitch angle of 23.9 deg at 75% of the radius. Reference [17] provides the radial distributions of the blade chord and twist angle. The axisymmetric nacelle, connected directly to the wing, has a diameter of 0.070 m.

Compared to modern designs, the propeller has a low blade count, a low solidity, and no sweep. Yet, its slipstream introduced the relevant aerodynamic phenomena to the flowfield that affect the propeller-wing interaction. Therefore, it was decided that the propeller was adequate for the study presented in this paper.

© 2019 by T. Sinnige, T. C. A. Stokkermans, N. van Arnhem, and L. L. M. Veldhuis.
https://doi.org/10.2514/6.2019-3033

2. Wing

A semi-installed propeller-wing configuration is simulated by combining the propeller and nacelle with a straight wing with a chord length of $c = 0.240$ m, a span of $s_w = 0.292$ m, a symmetric NACA 64_2A015 profile, and a 25%-chord plain flap with a flap gap of 1 mm. A low-aspect-ratio wing with a high ratio of propeller diameter to wingspan is used to obtain a strong interaction between the propeller slipstream and the wing, which aids in the interpretation of the aerodynamic interaction mechanisms. The distance between the propeller plane and the wing leading edge is 44% of the propeller diameter. Transition was forced in the experiment using strips with silicon-carbide particles, at $x/c = 0.12$ on both the upper and lower sides of the wing. The numerical simulations were fully turbulent.

The flap is used to simulate the cases with the propeller slipstream rotating in the same and opposite directions of the wingtip vortex (outboard-up and inboard-up propeller rotation) with a single propeller. This was achieved by performing the experimental and numerical simulations at symmetric positive and negative flap deflection angles (±10 deg). The results obtained at the negative flap setting represent the outboard-up rotating case at the positive flap setting after inverting the sign of the angle of attack and the lift coefficient:

$$\begin{aligned} \alpha_{\mathrm{OU}} &= -\alpha_{\mathrm{IU}}, \\ C_{L_{\mathrm{OU}}} &= -C_{L_{\mathrm{IU}}}, \\ C_{D_{\mathrm{OU}}}(C_{L_{\mathrm{OU}}}) &= C_{D_{\mathrm{IU}}}(-C_{L_{\mathrm{IU}}}). \end{aligned} \tag{1}$$

B. Wind-Tunnel Experiment

The experimental data were obtained with the same setup as discussed in detail in Ref. [2]. Here, only a summary is provided. The experiments were performed in the Low-Turbulence Tunnel at Delft University of Technology. This low-speed, closed-return wind tunnel features a closed-wall test section, visible in Fig. 2a, with a cross-section of 1.80×1.25 m. At the selected freestream velocity of 40 m/s, the turbulence level is below 0.1%. The models were attached to a ground board of 2.055 m length suspended from the test section's ceiling, spanning the entire width of the test section. This ground board represents the symmetry plane for the experimental arrangement, and reduced the height of the test section to 0.995 m. The flow on the ground board was made turbulent by a transition strip, applied at 0.140 m from the board's leading edge. The wing model was connected to the turntable integrated into the ground board, with the wing leading edge positioned at 1.205 m ($5.02c$) downstream of the ground board's leading edge.

The integral forces and moments generated by the propeller-wing combination were obtained with an external six-component balance. Measurements were taken both with and without the propeller blades installed to allow for an assessment of the aerodynamic interaction effects caused by the propeller slipstream. Apart from the forces acting on the models, the balance data also included the forces and moments on the turntable in the wind-tunnel ceiling (Fig. 2), mostly dominated by skin-friction drag. Tare measurements were taken with the model removed from the test section to correct for this effect. This approach cannot account for the interference drag associated with the junction flow at the interface between the wing and the turntable. The uncertainty of the balance measurements was estimated from repeated measurements at equal operating conditions. The typical standard deviation of the lift data is around 0.04 lift counts, while the standard deviation of the drag data is approximately 3 drag counts.

The wing model used in the experiment contains a total of 408 pressure taps (Fig. 2b), providing local measurements of the pressure distribution at 8 spanwise locations. For the operating conditions considered in this paper, data were recorded only at $y/s = 0.445$ and $y/s = 0.666$, corresponding to spanwise stations outside and inside the slipstream, respectively. The pressure data were integrated to obtain the section lift coefficient on the wing. In this process, the local geometry of the wing profile was accounted for.

C. CFD Simulations With RANS Solver

Steady simulations were performed for the propeller-wing configuration considered in the experiment using an actuator-disk approach. The blade-loading data required for these simulations was obtained from simulations of the isolated propeller configuration (blades, spinner, and nacelle). The latter simulations were performed by considering a single blade with spinner and nacelle in a 90-deg wedge. An overview of the corresponding domains and boundary conditions is shown in Fig. 3. Note that the simulations of the isolated propeller were done with far-field boundaries, while the simulations of the propeller-wing configuration were performed in the wind-tunnel domain, i.e. with the wind-tunnel walls modeled. As shown in Fig. 3, the inner domain could be positioned at an angle of attack with respect to the modeled wind-tunnel walls. This paper only discusses numerical results obtained at an angle of attack of 0 deg.

© 2019 by T. Sinnige, T. C. A. Stokkermans, N. van Arnhem, and L. L. M. Veldhuis.
https://doi.org/10.2514/6.2019-3033

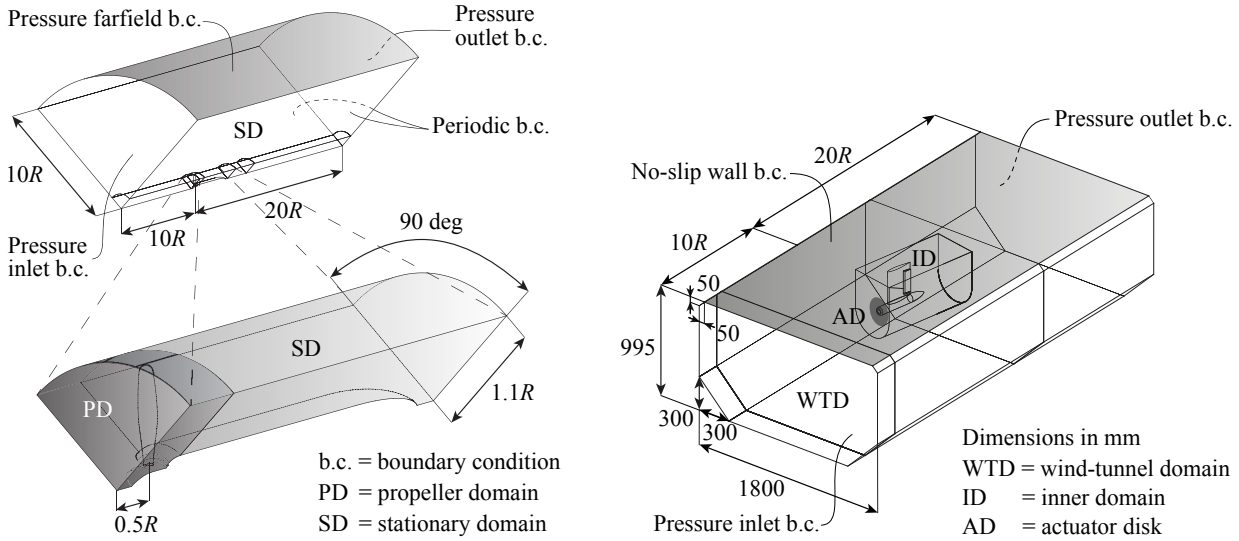

a) Isolated propeller **b) Propeller-wing configuration**

Fig. 3 Numerical domains and boundary conditions [18].

The numerical simulations were performed by solving the Reynolds-averaged Navier-Stokes equations for compressible flow with a second-order scheme using ANSYS® Fluent, Release 16.0[19], a commercial, unstructured, finite-volume, cell-centered solver. The advection term was discretized with an upwind scheme using the Barth-Jespersen boundedness principle [20]. Turbulence was modeled using the Spalart-Allmaras one-equation model [21], with modification proposed by Dacles-Mariani et al. [22] to prevent build-up of turbulence viscosity in vortex cores. The inlet turbulence quantities were selected following the recommendations by Spalart and Rumsey [23], resulting in an eddy viscosity ratio of 0.21044 with the wing chord as reference. To fully resolve the boundary layer, the y^+ value on the no-slip walls of the model was less than one.

A detailed discussion of the numerical setup, including grid-dependency studies, is provided in Ref. [18]. This reference also compares the actuator-disk results to data obtained from simulations with fully-resolved blades and simulations with an actuator-line model. The wing loading was nearly the same using these three numerical approaches, and the actuator-disk model provided a good prediction of the wing loads compared to the experimental data.

D. Low-Order Numerical Analyses With Blade-Element Method

The open-source blade-element tool XROTOR[24] was used to allow for rapid propeller loading predictions that were for example used to identify the optimal blade pitch setting of the propeller for maximum energy-harvesting performance. The XROTOR simulations were run with the built-in self-deforming wake model, and the wake-induced velocities computed with the available potential-flow method. XFOIL[25] was used to obtain the propeller blade section characteristics which are required as inputs to XROTOR. Multi-variable optimizations were performed to convert the raw lift and drag polars into the lift and drag response models employed by XROTOR. The airfoil data were not corrected for the effects of rotation on the blade section characteristics.

E. Test Cases

All results discussed in this paper were obtained with a freestream velocity of $V_\infty = 40$ m/s to remain consistent with the data set discussed in Ref. [2]. The resulting Reynolds number based on the wing chord was about $Re_c = 650{,}000$, while the Reynolds number based on the propeller diameter was $Re_D = 640{,}000$. The measurements were performed over an angle-of-attack range of $-20 \leq \alpha \leq 20$ deg, while the numerical simulations were only performed with symmetric inflow conditions ($\alpha = 0$ deg). Tare measurements and simulations were performed with the blades removed to obtain a baseline to which the propeller-on data could be compared. The propeller was operated around negative thrust conditions, corresponding to advance ratios in the range of $1.0 \leq J \leq 1.8$ at the selected blade pitch of 23.9 deg at $r/R = 0.75$. The corresponding Reynolds number referenced to the chord length and effective velocity on the outboard part of the blades was around 100,000. Measurement cases at positive thrust setting were evaluated before, and are discussed extensively in Ref. [2]. These data are included in the paper in order to compare the response at positive and negative thrust settings.

© 2019 by T. Sinnige, T. C. A. Stokkermans, N. van Arnhem, and L. L. M. Veldhuis.
https://doi.org/10.2514/6.2019-3033

III. Results

The performance of the isolated propeller was analyzed using the CFD simulations with single blade (Sec. II.C) and the XROTOR analyses (Sec. II.D). The interaction effects for the propeller-wing configuration were investigated based on the experiments (Sec. II.B) and the CFD simulations with actuator-disk model (Sec. II.C).

A. Isolated Propeller Performance

1. Blade Loading

Figure 4 displays the performance of the isolated propeller in terms of thrust and torque coefficient versus advance ratio. The data were obtained from the CFD simulations of the isolated propeller and XROTOR. The qualitative agreement between the CFD and XROTOR data is reasonable. The quantitative offset in thrust and especially power between the two data sets is most likely due to inaccuracies in the lift and drag data of the blade sections used in the XROTOR analyses. Figure 4a provides the thrust and power coefficients referenced to the rotational speed of the propeller ($C_T = T/\rho_\infty n^2 D^4$ and $C_P = P/\rho_\infty n^3 D^5$). For the installed configuration, the thrust coefficient of the rotor C_T does not relate directly to the interaction effects at the wing. Therefore, in Sec. III.B the alternative definition of the thrust coefficient, $T_C = T/q_\infty D^2$, is used. This coefficient represents the average disk loading over the actuator disk. For reference, Fig. 4b plots T_C as a function of the advance ratio, again based on both the CFD and XROTOR data.

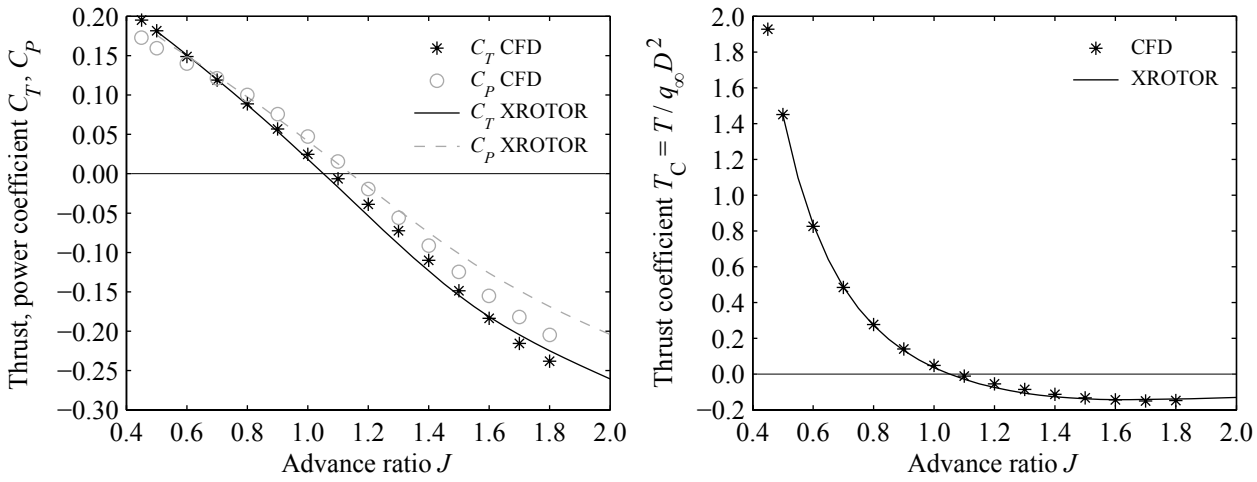

a) Referenced to rotational speed (C_T, C_P) **b) Referenced to freestream dynamic pressure (T_C)**

Fig. 4 Isolated propeller thrust and power coefficient versus advance ratio.

The propeller response at positive thrust shown in Fig. 4a is as expected and was described in Ref. [2]. From an advance ratio of approximately 1.0 onward, the thrust becomes negative. In this regime, the lift and drag forces on the blade sections both contribute to the force in the thrust direction (Fig. 1). Therefore, the slope of the thrust coefficient C_T versus advance ratio steepens compared to that in positive-thrust conditions. The propeller power coefficient displays a comparable trend as the thrust coefficient, even though in the negative-thrust regime the drag force opposes the negative torque. The cross-over advance ratio from positive to negative power occurs at higher advance ratio than for the thrust. This is because the lift coefficients are small but positive at the zero thrust condition, thus contributing to a positive torque. For advance ratios above approximately 1.4, the thrust and power response flatten, because the cambered airfoil sections of the considered propeller are not designed for operation at relatively large negative angles of attack. This was also observed in previous work for windmilling fans [16], and is caused by local separation on the blades.

To visualize the differences in flow separation on the blades between typical propulsive and energy-harvesting conditions, Fig. 5 plots distributions of skin friction coefficient and shearlines on the blades at $J = 0.8$ and $J = 1.6$. Note that the colorbars in the two subfigures do not have the same scale. It can be seen that the cambered blade sections are not efficient for operation at negative loading conditions. In propulsive mode (Fig. 5a), the flow is attached over the largest part of the blade, except for trailing-edge stall on the inboard radial sections. This is due to the locally inefficient blade design, and would not occur on more modern blade designs at comparable conditions. In energy-harvesting mode (Fig. 5b), additional flow separation can be observed near the trailing edge of the blade at about 40% and 90% of the radius. Shape optimization would be required to make the blade design more robust for efficient energy harvesting.

© 2019 by T. Sinnige, T. C. A. Stokkermans, N. van Arnhem, and L. L. M. Veldhuis.
https://doi.org/10.2514/6.2019-3033

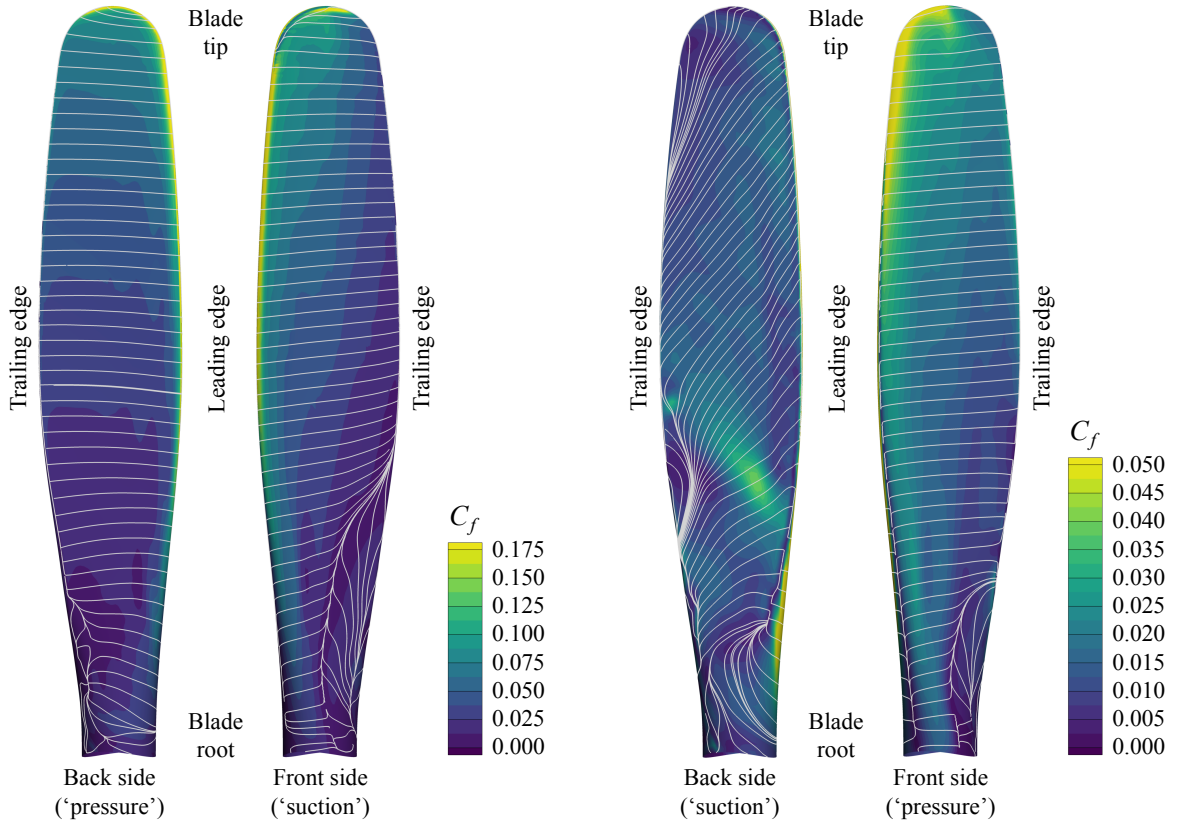

a) Propulsive mode ($J = 0.8, C_T = 0.09$) **b) Energy-harvesting mode ($J = 1.6, C_T = -0.18$)**

Fig. 5 Visualization of flow separation on the propeller blades by contours of skin friction coefficient and shear lines (CFD data).

The high negative thrust and torque (power) on the blades and associated separation in energy-harvesting conditions leads to local distortions in the blade loading distributions. This is shown in Fig. 6 for the radial distributions of thrust and power. At negative thrust conditions, the shape of the loading distributions clearly differs from the typical result for minimum-induced loss in the positive thrust regime. Moreover, the flattening of the blade response at high advance ratio, observed before in Fig. 4a, can clearly be recognized when for example comparing the blade loading distributions at $J = 1.6$ and $J = 1.8$.

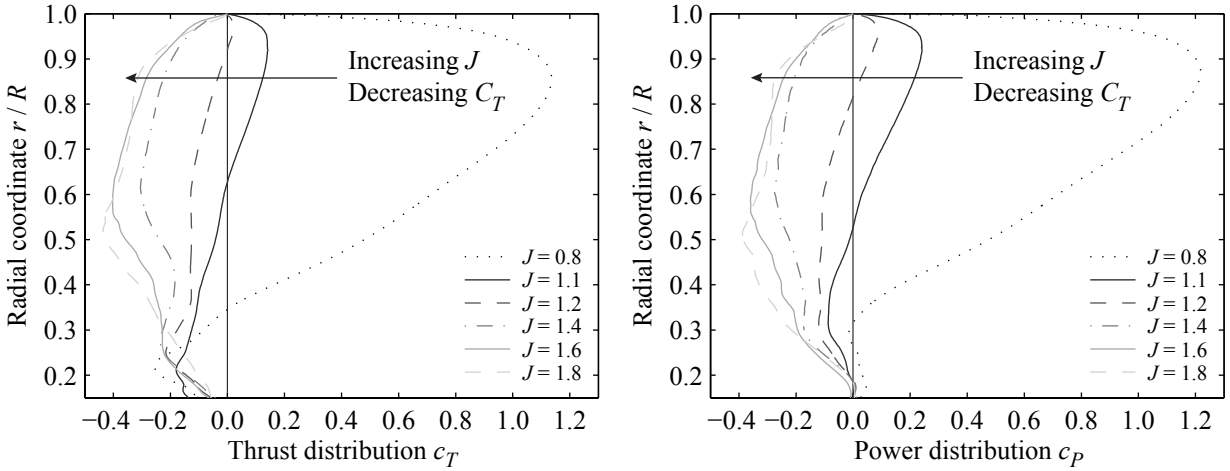

a) Thrust **b) Power**

Fig. 6 Blade loading distributions (CFD data).

© 2019 by T. Sinnige, T. C. A. Stokkermans, N. van Arnhem, and L. L. M. Veldhuis.
https://doi.org/10.2514/6.2019-3033

2. Slipstream Characteristics

The distorted blade-loading distribution affects the slipstream characteristics and thus the interaction effects on a downstream aerodynamic surface immersed in the slipstream. Figure 7 provides the radial distributions of axial and tangential velocity in the slipstream at $0.19R$ downstream of the propeller center. These distributions are instrumental in the interpretation of the data for the propeller-wing configuration. The edge of the nacelle is located at $r/R = 0.295$.

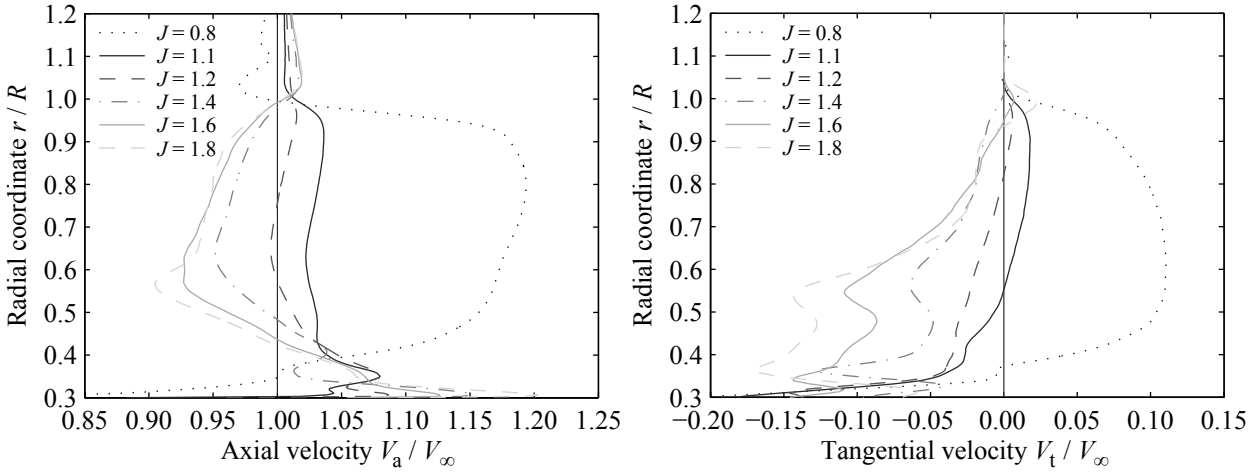

a) Axial velocity **b) Tangential velocity**

Fig. 7 Radial distributions of axial and tangential velocity in the propeller slipstream at $0.19R$ downstream of the propeller center (CFD data).

The distribution of the axial velocity (Fig. 7a) displays the expected decrease in velocity with decreasing thrust setting (increasing advance ratio). At negative loading conditions, the axial velocity in the slipstream is lower than in the freestream. This will cause a decrease in the lift on surfaces immersed in the slipstream. Comparing the results at positive and negative power coefficients (for example $J = 0.8$ versus $J = 1.6$), it can be seen that the tangential velocity (Fig. 7b) reverses. This is as expected considering the opposite direction of the propeller torque in both conditions. Since the tangential velocity in the slipstream modifies the effective angle of attack perceived by the downstream wing, this will have a pronounced impact on the wing loading of the installed configuration.

3. Energy-Harvesting Performance

The power coefficient used in Figs. 4 and 6 does not provide a clear insight into the absolute power consumption or generation by the propeller. Therefore, an alternative power coefficient, $P_C = P/\rho_\infty V_\infty^3 D^2$, was defined to assess the energy-harvesting performance of the propeller. Furthermore, an energy-harvesting efficiency was defined as:

$$\eta_{eh} = \frac{P}{\frac{1}{2}\rho_\infty \pi R^2 V_\infty^3}, \tag{2}$$

with P the power generated by the rotor (obtained directly from CFD and XROTOR), and the term in the denominator representing the power available in the flow for energy conversion, defined following the typical convention for horizontal-axis wind turbines. Figure 8 displays the corresponding results from CFD and XROTOR. It can be seen that in both cases maximum regenerative power and energy-harvesting efficiency is obtained around $J = 1.6$, with the CFD and XROTOR results again in qualitative agreement over the entire advance-ratio range considered. The XROTOR simulations underestimate the regenerative power compared to CFD, leading to an energy-harvesting efficiency lower by about 2 percentage points. At the considered blade pitch setting, the maximum energy-harvesting efficiency predicted by the CFD data was about 10%. This is low compared to modern large-scale horizontal-axis wind turbines, for which values of up to around 50% can be reached [26]. For small wind turbines the efficiency is already considerably lower due to the reduction in lift-to-drag ratio of the blade sections with decreasing Reynolds number [26]. Furthermore, the propeller used for the analyses discussed in this paper was not designed for operation at negative thrust conditions. Therefore, the energy-harvesting efficiency could be improved by changing the blade design, while taking into account that the propulsive performance should not be degraded. Ref. [12] has already proven the potential success of such a multi-objective design effort, in that case applied to a fixed-pitch energy-harvesting propeller on a small electric aircraft.

© 2019 by T. Sinnige, T. C. A. Stokkermans, N. van Arnhem, and L. L. M. Veldhuis.
https://doi.org/10.2514/6.2019-3033

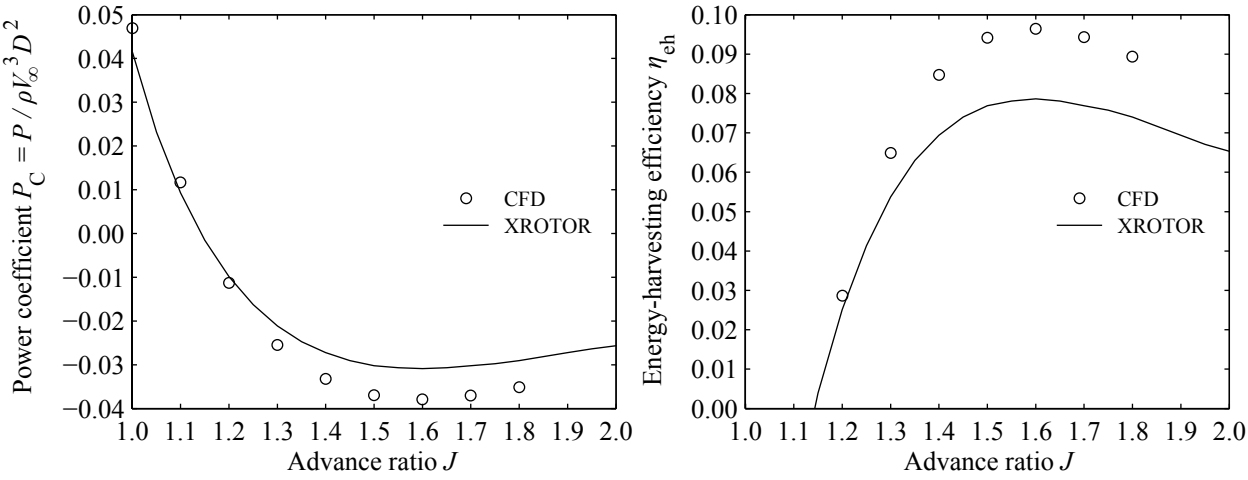

a) Power **b) Efficiency**

Fig. 8 Energy-harvesting performance by the propeller.

For a given blade design, the blade pitch setting can also be changed to obtain better energy-harvesting performance. To minimize the downtime during the experiment and the number of simulations, it was decided to consider a single blade pitch setting only for all test cases with propeller on. To investigate whether this choice was acceptable, advance-ratio sweeps were performed with XROTOR to obtain the propeller performance at four different pitch settings. Figure 9 plots the resulting sensitivity of the energy-harvesting efficiency (Eq. 2) versus blade pitch angle and advance ratio.

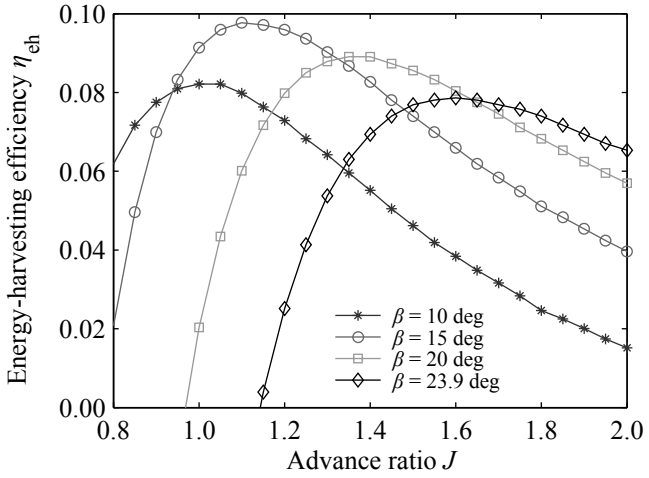

Fig. 9 Sensitivity of energy-harvesting performance to blade pitch setting (XROTOR data).

The results shown in Fig. 9 confirm the change in propeller response with blade pitch setting, and indicate that an optimal pitch setting exists for maximum energy-harvesting performance. For the propeller considered here, this pitch angle was approximately $\beta = 15$ deg, with a maximum energy-harvesting efficiency of about 10% as predicted by XROTOR. Note that Fig. 8b showed that the energy-harvesting efficiency was underpredicted by XROTOR compared to CFD by about 2 percentage points. The optimal pitch setting and maximum energy-harvesting efficiency will depend on the propeller design and the inflow conditions. As mentioned already, the tested propeller was not optimized for maximum energy-harvesting performance. According to the results discussed in Ref. [12], the maximum regenerative power could be increased by increasing the solidity.

Since the considered propeller was not optimized for maximum energy harvesting or minimum negative thrust in windmilling conditions, the quantitative differences between the various pitch angles are considered irrelevant for this paper. The focus is on understanding the interaction phenomena at the wing due to the incoming slipstream of a propeller that generates negative thrust. In a qualitative sense, the propeller response is similar at the different pitch settings. Therefore, the fixed pitch angle selected in the experiment and the CFD simulations will not hinder the investigation of the interaction phenomena relevant to tip-mounted tractor propellers in negative-thrust conditions.

© 2019 by T. Sinnige, T. C. A. Stokkermans, N. van Arnhem, and L. L. M. Veldhuis.
https://doi.org/10.2514/6.2019-3033

B. Installed Performance

The negative thrust produced by the propeller in windmilling and energy-harvesting conditions causes a drastic modification of the propeller-airframe interactions compared to the propulsive case. This was investigated using the experimental data and the numerical data extracted from the actuator-disk simulations. The validity of the simulation approach was shown before in Refs. [18, 27] and is, therefore, not discussed in the present paper.

1. Integrated Loading

An external balance was used to measure the lift and drag of the propeller-wing configuration in the experiment. Figure 10 presents the resulting lift and drag polars for a selection of the considered operating conditions. The case without propeller installed is taken as baseline, to which the propeller-on data with inboard-up rotation are compared. Two propulsive conditions are included; these data were published before in Ref. [2]. Furthermore, two negative-thrust conditions are shown, one close to a free windmilling condition ($J = 1.2$, $T_C = -0.05$), and one corresponding to the optimal energy-harvesting condition ($J = 1.6$, $T_C = -0.14$). For overview reasons, the drag polars are only displayed for the propeller-off, $J = 0.9$, and $J = 1.6$ cases. Note that the balance measured the forces generated by the entire model, including the propeller. Therefore, the propeller thrust and normal forces are included in the recorded lift and drag forces. The reference area used throughout the paper to nondimensionalize lift and drag data was based on the span of the wing with nacelle (0.362 m).

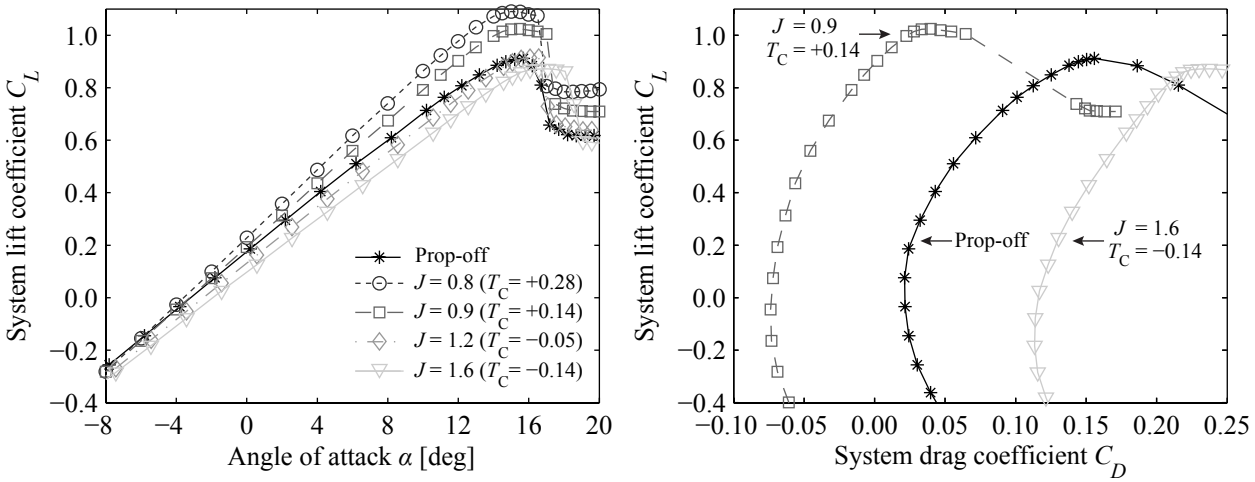

Fig. 10 Effect of propeller thrust setting on the integrated loading of the propeller-wing configuration (experimental data).

As expected, the system lift (Fig. 10a) decreases with decreasing propeller thrust setting. The associated reduction in axial velocity, hence dynamic pressure, in the slipstream (Fig. 7a) lowers the local lift on the part of the wing immersed in the slipstream. With inboard-up rotation, this is further enhanced by the reversed swirl in the slipstream that occurs at negative power setting (Fig. 7b), following the mechanism sketched in Fig. 11. The results at $J = 1.2$ are very similar to those recorded for the blades-off case. This is due to the small thrust and torque produced by the propeller at $J = 1.2$ (Fig. 4) and associated small propeller-induced velocities (Fig. 7). As a result, the offset in propeller forces with respect to the blades-off configuration is small, and the interaction effects at the wing are minimal.

The drag polars (Fig. 10b) display large differences between the considered test cases. This is mostly because the propeller thrust is included in the presented system forces. Compared to the blades-off case, the propeller generates negative thrust (i.e. additional drag) in energy-harvesting conditions. Therefore, the drag polars at these operating conditions are shifted to the right, as illustrated in Fig. 10b for the case at $J = 1.6$. In this condition, the system performance especially improved at negative lift coefficient. This is due to a combination of the reduced dynamic pressure experienced by the wing on the part washed by the slipstream, beneficial tip-vortex-attenuation and swirl-recovery effects due to the reversed swirl in the slipstream (as discussed for the propulsive case at positive lift in Ref. [2]), and the modification of the propeller blade forces at nonzero angle of attack. With increasing angle of attack (absolute value), the propeller thrust increases and thus becomes less negative in the energy-harvesting condition. As a result, the apparent lift-induced drag of the complete system then decreases compared to the propeller-off case.

© 2019 by T. Sinnige, T. C. A. Stokkermans, N. van Arnhem, and L. L. M. Veldhuis.
https://doi.org/10.2514/6.2019-3033

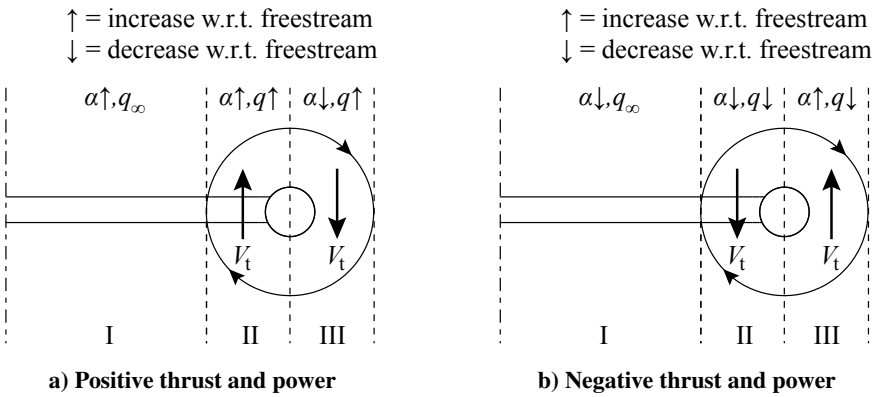

a) Positive thrust and power **b) Negative thrust and power**

Fig. 11 Effect of the propeller-induced velocities experienced by the wing for the inboard-up rotation case.

The system performance of vehicles with wingtip-mounted tractor propellers strongly depends on the rotation direction of the propeller [2]. When operating the propeller at negative thrust and power, the slipstream velocities reverse compared to the conventional propulsive mode (Fig. 7). Consequently, the effect of the propeller rotation direction is different in the propulsive and energy-harvesting modes. Figure 12 compares the effect of the propeller rotation direction on the system lift and drag between the two modes of propeller operation. Again, the propeller forces are included in the lift and drag data. For ease of interpretation, the lift data are cross-plotted against the thrust coefficient T_C at three angles of attack. The drag data are presented in the same way as in Fig. 10b.

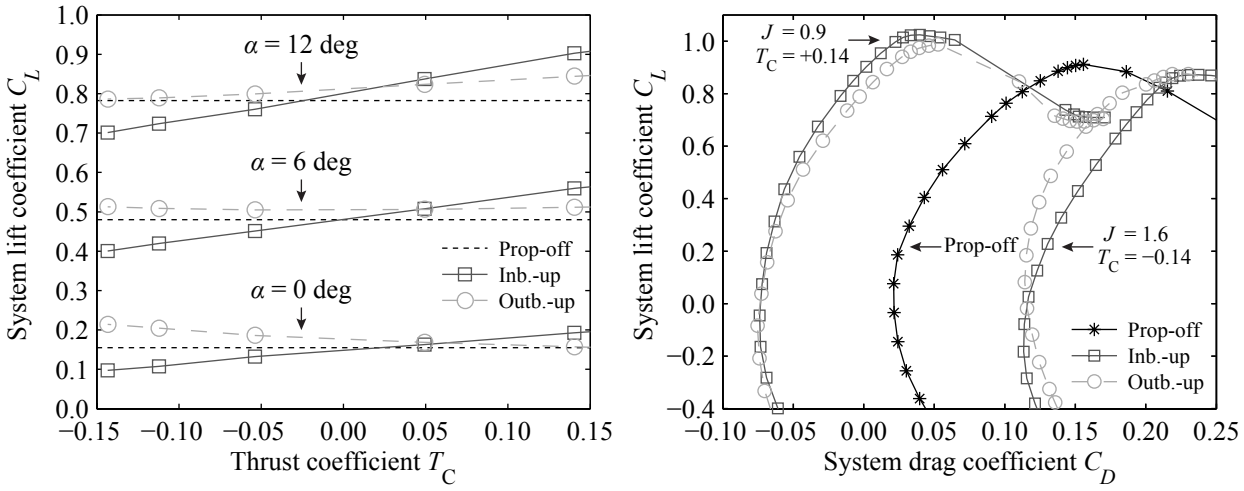

a) Lift **b) Drag**

Fig. 12 Effect of propeller rotation direction on the integrated forces generated by the propeller-wing configuration (experimental data).

As expected, the effect of the rotation direction on the system loading is a function of the thrust coefficient, and thus reverses between the propulsive and energy-harvesting modes. At positive wing lift, swirl recovery and tip-vortex attenuation occur when the tangential velocity in the slipstream increases the effective angle of attack at the wing sections. In propulsive mode, this occurs with inboard-up propeller rotation [2]. In energy-harvesting conditions, the tangential velocity in the slipstream is opposite to that in propulsive mode (Fig. 7b). Therefore, the optimal rotation direction is also opposite to that in propulsive mode, and the vehicle performance increases with outboard-up rotation. In terms of lift this is clearly illustrated by Fig. 12a, while the reduction in induced drag can be seen from Fig. 12b. Compared to the propulsive mode, the reduction in axial velocity in the slipstream in energy-harvesting mode at least partially offsets the beneficial effect due to swirl. Therefore, the system performance enhancement by the propeller is typically smaller than in the propulsive mode. The relative magnitude of the propeller-induced effects depends on the ratio of axial and tangential velocity in the slipstream, and thus is a configuration-specific result.

© 2019 by T. Sinnige, T. C. A. Stokkermans, N. van Arnhem, and L. L. M. Veldhuis.
https://doi.org/10.2514/6.2019-3033

2. Wing Loading

To provide additional insight into the local effects of the propeller slipstream on the wing loading, the sectional loading characteristics were extracted. Estimates of the local wing lift were obtained from the experimental data by integrating the measured surface pressure distributions. These results may be affected by the coarse resolution of the pressure taps on the wind-tunnel model, especially around the flap. The pressure and skin-friction data from the CFD simulations were integrated to obtain both lift and drag distributions over the entire wing. Figure 13 presents the results at positive and negative thrust coefficient, in terms of section lift coefficient and corresponding lift-to-drag ratio. The markers indicate the experimental data. The spanwise coordinate was made dimensionless with the wing span of 0.292 m, starting from zero at the root of the model. The loading on the nacelle is thus not shown in the figure. Note that the $J = 0.8$ case is used in Fig. 13 to represent the results in propulsive mode of the propeller, since no simulations were performed for the case at $J = 0.9$. Furthermore, it should be taken into account that the different operating conditions considered in Fig. 13 did not lead to the same wing lift coefficient.

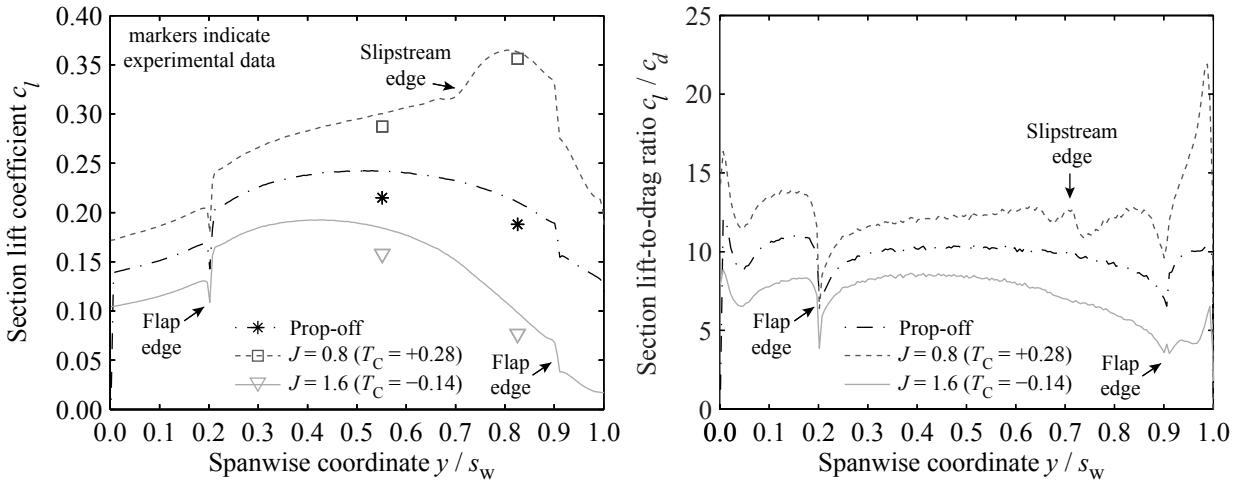

a) Lift distribution **b) Lift-to-drag distribution**

Fig. 13 Effect of propeller thrust setting (inboard-up rotation) on the wing loading distribution at $\alpha = 0$ deg (CFD and experimental data).

The wing lift distributions (Fig. 13a) follow the trends observed before for the system lift (Fig. 10a). The reduced axial velocity in the slipstream of the propeller at negative thrust results in a drop in wing lift compared to the propeller-off condition, which is amplified by the downwash induced by the propeller swirl for the considered inboard-up rotation case. A comparable similarity was observed in the experimental data set between the wing lift and system lift at nonzero angle of attack, both inside and outside of the slipstream. This shows that the interaction of the propeller slipstream with the wing plays a dominant role in the performance of the propeller-wing combination, as expected based on the results for the propulsive mode discussed in Ref. [2]. Qualitatively, the polars of system lift and section lift were the same; therefore, the latter are omitted here.

As observed in previous work [27], the CFD simulations return a higher section lift coefficient than that obtained from the experiment, but the trends were captured at all thrust settings. As mentioned, the experimental results will be affected by the finite resolution of the pressure data available for integration, possibly explaining part of the offset.

The changes in lift-to-drag performance of the wing with the propeller thrust coefficient (Fig. 13b) also mimic those observed for the complete system (Fig. 10b). With inboard-up rotation, the upwash on the wing leads to enhanced performance in propulsive mode, while the corresponding downwash in energy-harvesting mode decreases the performance compared to the propeller-off configuration. The resulting change in wing lift-to-drag ratio was assessed by integrating the spanwise distribution (excluding the nacelle). Figure 14 provides the resulting lift-to-drag ratios of the wing as a function of thrust coefficient T_C, for both inboard-up and outboard-up rotation. The datapoints in Fig. 14 were all obtained at $\alpha = 0$ deg, and thus are not at constant wing lift coefficient. For reference, the wing lift coefficients corresponding to each datapoint are indicated in the figure.

© 2019 by T. Sinnige, T. C. A. Stokkermans, N. van Arnhem, and L. L. M. Veldhuis.
https://doi.org/10.2514/6.2019-3033

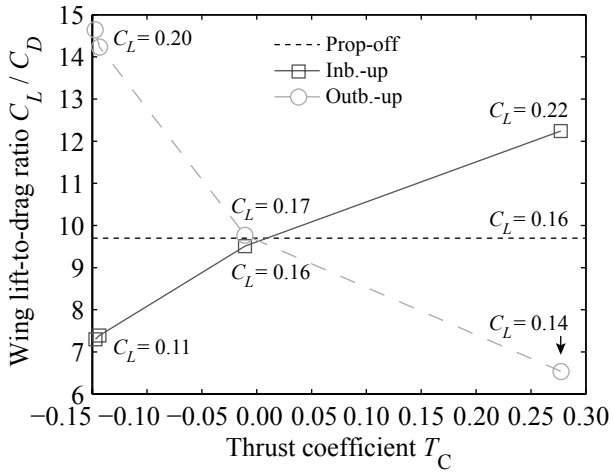

Fig. 14 Effect of propeller thrust setting on the wing lift-to-drag ratio at α = 0 deg (CFD data).

Figure 14 shows that the wing lift-to-drag ratio increased by about 25% when compared to the propeller-off configuration for the case with inboard-up rotation and the propeller in propulsive mode at a thrust coefficient of $T_C = 0.28$ ($J = 0.8$). With the same rotation direction in negative thrust conditions, on the other hand, the lift-to-drag ratio decreased by about 25% compared to the propeller-off result at thrust coefficients of about $T_C = -0.15$ ($J = 1.6$ to 1.8). At a condition of zero thrust (around $J = 1.1$), the propeller effect is negligible, as expected.

An opposite trend is observed for the case with outboard-up rotation. At positive thrust, the wing lift-to-drag ratio decreased by around 30% at $T_C = 0.28$ ($J = 0.8$). Due to the reversed swirl in the negative thrust regime, the wing lift-to-drag ratio increased with decreasing propeller thrust. At a thrust coefficient of $T_C = -0.15$ ($J = 1.6$ to 1.8), the increase in lift-to-drag ratio was near 50%. Note that this benefit is larger than the increase observed with inboard-up rotation in the positive thrust regime. This can partially be attributed to the different wing lift coefficients. Moreover, the reduced dynamic pressure in the slipstream of the energy-harvesting propeller will reduce the friction drag on the wing compared to the propulsive case.

3. Slipstream Flowfields

The effect of the propeller thrust condition on the slipstream flowfields was assessed using the CFD data. Two survey planes were considered. The first was positioned at $0.19R$ downstream of the propeller center to assess the initial slipstream flowfield. A second survey plane was defined at 1.5 wing chord lengths downstream of the wing trailing edge, corresponding to an axial location of $5.9R$ downstream of the propeller center. Figure 15 plots the computed swirl-angle distribution in both planes as a function of the propeller operating condition for the case with inboard-up rotation. Figure 16 plots the same quantity for the outboard-up rotation case.

Figures 15 and 16 display the expected change in swirl in the downstream plane at positive thrust. With inboard-up rotation the swirl decreases, while with outboard-up rotation the swirl increases, as shown before in Ref. [2] with experimental data. The results at negative thrust setting confirm the reversal of the interaction effects in the energy-harvesting condition that were observed in the loading data discussed in the previous sections. The distortion of the slipstream [2] was smaller in the negative-thrust condition than in propulsive mode. This is expected to be a consequence of the smaller distortion of the spanwise wing lift distribution (Fig. 13a) in the energy-harvesting condition.

The swirl-angle distributions were integrated to obtain a single figure of merit for each configuration, using the following equation:

$$\theta_{\text{int}} = \frac{1}{A_{\text{ref}}} \int_0^{2\pi} \int_0^{1.1R} \theta r \, \mathrm{d}r \, \mathrm{d}\phi, \tag{3}$$

with $A_{\text{ref}} = \pi(1.1R)^2 - \pi R_{\text{nac}}^2$ for the upstream survey plane (hence with the area inside the nacelle removed) and $A_{\text{ref}} = \pi(1.1R)^2$ for the downstream survey plane. The radial integration limit was set to $1.1R$ to capture the entire slipstream, also in cases with slipstream distortion resulting from the interaction with the wing. The resulting mean swirl angles are summarized in Table 1.

© 2019 by T. Sinnige, T. C. A. Stokkermans, N. van Arnhem, and L. L. M. Veldhuis.
https://doi.org/10.2514/6.2019-3033

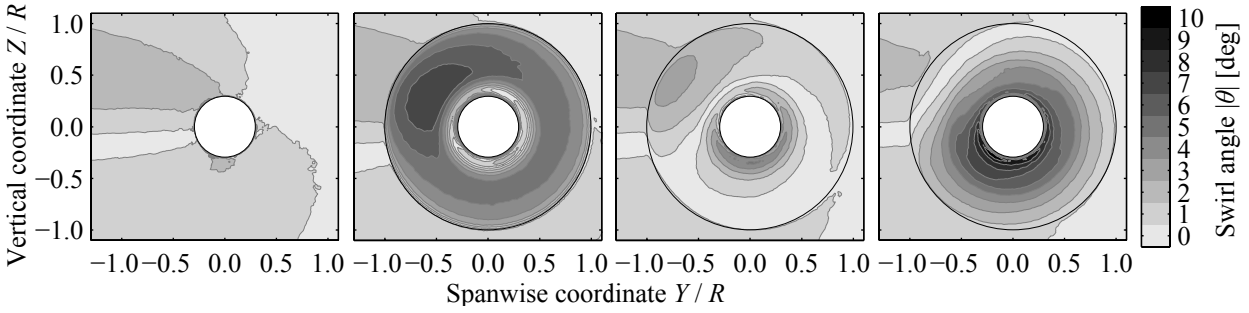

a) Propeller-off, upstream **b) $J = 0.8, T_C = +0.28$, upstream** **c) $J = 1.1, T_C = -0.01$, upstream** **d) $J = 1.6, T_C = -0.14$, upstream**

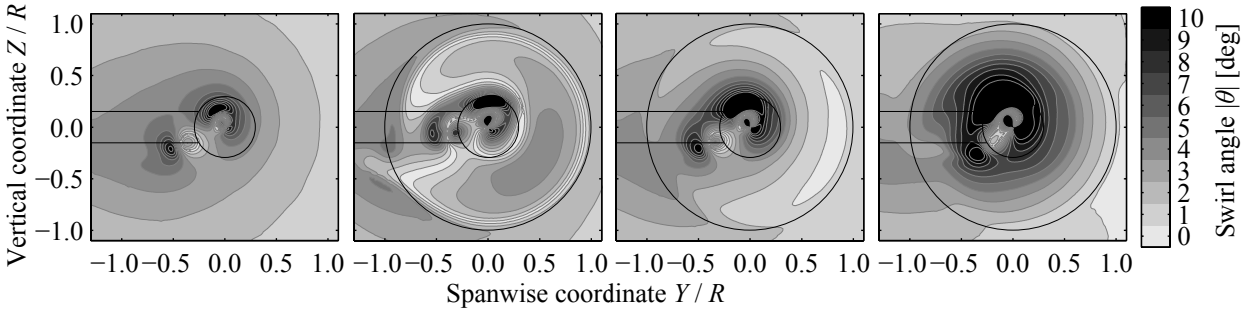

e) Propeller-off, downstream **f) $J = 0.8, T_C = +0.28$, downstream** **g) $J = 1.1, T_C = -0.01$, downstream** **h) $J = 1.6, T_C = -0.14$, downstream**

Fig. 15 Effect of propeller thrust setting on the swirl-angle distribution upstream and downstream of the wing with inboard-up rotation at $\alpha = 0$ deg (CFD data).

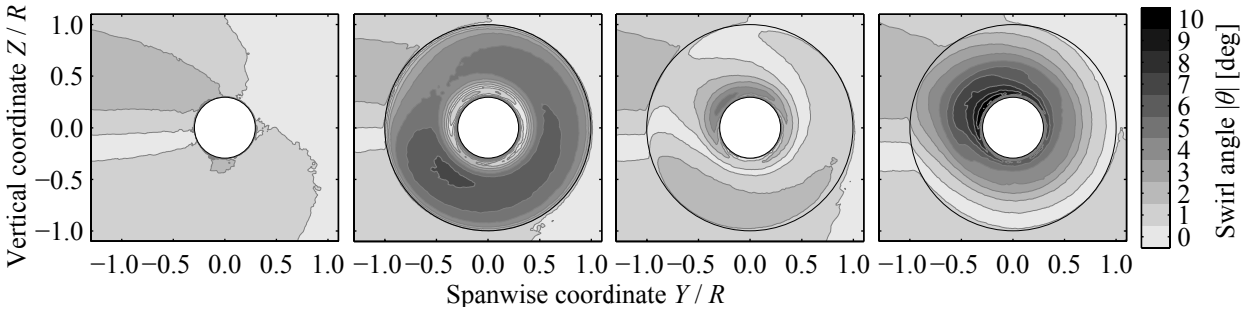

a) Propeller-off, upstream **b) $J = 0.8, T_C = +0.28$, upstream** **c) $J = 1.1, T_C = -0.01$, upstream** **d) $J = 1.6, T_C = -0.14$, upstream**

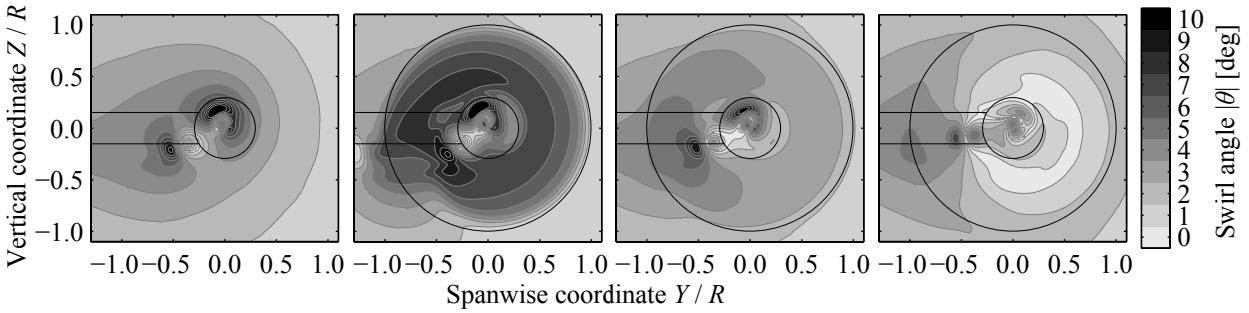

e) Propeller-off, downstream **f) $J = 0.8, T_C = +0.28$, downstream** **g) $J = 1.1, T_C = -0.01$, downstream** **h) $J = 1.6, T_C = -0.14$, downstream**

Fig. 16 Effect of propeller thrust setting on the swirl-angle distribution upstream and downstream of the wing with outboard-up rotation at $\alpha = 0$ deg (CFD data).

© 2019 by T. Sinnige, T. C. A. Stokkermans, N. van Arnhem, and L. L. M. Veldhuis.
https://doi.org/10.2514/6.2019-3033

Table 1 Effect of propeller rotation direction and thrust setting on the mean swirl angle in the wake of the propeller-wing model at α = 0 deg (CFD data).

Operating point		C_L		$\theta_{\text{int}}^{\text{ups}}$		$\theta_{\text{int}}^{\text{dwns}}$	
J	T_C	Inboard-up	Outboard-up	Inboard-up	Outboard-up	Inboard-up	Outboard-up
Prop-off	-	0.16	0.16	0.0 deg	0.0 deg	−3.0 deg	−3.0 deg
0.8	+0.28	0.22	0.14	3.3 deg	−3.3 deg	−0.3 deg	−5.2 deg
1.1	−0.01	0.16	0.17	0.1 deg	−0.2 deg	−2.7 deg	−3.1 deg
1.6	−0.14	0.11	0.20	−2.3 deg	+2.3 deg	−4.5 deg	−1.5 deg

Table 1 shows that with inboard-up rotation, the positive swirl in the propeller slipstream at $T_C = 0.28$ ($J = 0.8$) (see upstream result) canceled the negative swirl induced by the wing (see downstream propeller-off result), resulting in a near zero average swirl. At $T_C = -0.14$ ($J = 1.6$), on the other hand, the negative swirl in the propeller slipstream added to the negative swirl induced by the wing, thus leading to an increase in the absolute swirl angle compared to the propeller-off result. With outboard-up rotation, the results are reversed. At positive thrust, the swirl angle downstream of the propeller-wing configuration increases compared to the propeller-off condition, while with negative thrust the swirl decreases. These results are consistent with the induced-drag data shown in Fig. 12b, and once more highlight the sensitivity of the system performance to the propeller rotation direction.

IV. Conclusions

This paper has quantified and explained the performance of an isolated propeller in energy-harvesting conditions, the resulting system performance of a tip-mounted propeller-wing configuration, and the local loading on the wing as a function of propeller thrust setting. For the isolated propeller configuration, the following conclusions are drawn:

- In the negative thrust regime, both the lift and drag forces acting on the blade sections contribute to the force in the thrust direction. Consequently, the slope of the thrust coefficient with advance ratio is higher than in the positive thrust regime. At constant freestream conditions and blade pitch setting, the absolute disk loading is much smaller in the negative-thrust regime because of the lower effective velocity at the blade sections.
- Beyond a certain advance ratio, the negative thrust and torque responses flatten to a smaller gradient with advance ratio than in positive-thrust conditions. The cambered airfoil sections of the considered propeller are not optimized for operation at relatively large negative angles of attack, thus causing separation and associated viscous losses.
- Maximum energy-harvesting performance is obtained at a unique blade pitch setting that depends on propeller design and inflow conditions, and thus is configuration specific. For the present propeller, not optimized for energy harvesting, this was at about 15 deg, providing an energy-harvesting efficiency of around 10%.
- The blade-loading distributions in negative-thrust conditions differ considerably from those typical of minimum-induced-loss propellers at positive thrust. This affects the slipstream characteristics and thus the interaction effects on the downstream wing.

For the wing-installed configuration, the aerodynamic interaction phenomena change drastically compared to the conventionally studied case at positive thrust setting. Based on analysis of the experimental and CFD data obtained for this configuration, the following conclusions are drawn:

- With inboard-up rotation, the system lift and drag performance worsen with increasingly negative propeller thrust setting. This is due to the reduced dynamic pressure in the propeller slipstream compared to the freestream, and the reversal of the swirl compared to the conventional case with positive thrust. Whereas in the propulsive condition studied in this paper ($T_C = 0.28$) the wing lift-to-drag ratio increased by about 25% compared to the propeller-off case, in energy-harvesting mode ($T_C = -0.14$) a reduction of 25% was observed. Note that these numbers are configuration specific.
- With outboard-up rotation, the interaction phenomena are reversed compared to the inboard-up rotation case. Improved wing performance can be achieved at negative thrust conditions. A maximum increase in wing lift-to-drag ratio of near 50% was obtained compared to the propeller-off case, albeit not at constant lift coefficient.
- The distortion of the slipstream is smaller at negative thrust conditions than at positive thrust conditions. This is due to the associated smaller distortion of the wing lift distribution at negative thrust conditions.

The novel results presented in this paper increase our understanding of a previously unexplored, yet relevant operating regime of the wingtip-mounted propeller. This understanding is useful for the further development of future electric aircraft.

© 2019 by T. Sinnige, T. C. A. Stokkermans, N. van Arnhem, and L. L. M. Veldhuis.
https://doi.org/10.2514/6.2019-3033

References

[1] Moore, M. D., and Fredericks, B., "Misconceptions of Electric Propulsion Aircraft and their Emergent Aviation Markets," *52nd Aerospace Sciences Meeting*, AIAA Paper 2014-0535, Jan. 2014. doi:10.2514/6.2014-0535.

[2] Sinnige, T., van Arnhem, N., Stokkermans, T. C. A., Eitelberg, G., and Veldhuis, L. L. M., "Wingtip-Mounted Propellers: Aerodynamic Analysis of Interaction Effets and Comparison with Conventional Layout," *Journal of Aircraft*, Vol. 56, No. 1, 2019, pp. 295–312. doi:10.2514/1.C034978.

[3] Snyder, M. H., Jr., and Zumwalt, G. W., "Effects of Wingtip-Mounted Propellers on Wing Lift and Induced Drag," *Journal of Aircraft*, Vol. 6, No. 5, 1969, pp. 392–397. doi:10.2514/3.44076.

[4] Miranda, L. R., and Brennan, J. E., "Aerodynamic Effects of Wingtip-Mounted Propellers and Turbines," *4th Applied Aerodynamics Conference*, AIAA Paper 1986-1802, June 1986. doi:10.2514/6.1986-1802.

[5] Stoll, A. M., Bevirt, J., Moore, M. D., Fredericks, W. J., and Borer, N. K., "Drag Reduction Through Distributed Electric Propulsion," *14th AIAA Aviation Technology, Integration, and Operations Conference*, AIAA Paper 2014-2851, June 2014. doi:10.2514/6.2014-2851.

[6] Borer, N. K., Patterson, M. D., Viken, J. K., Moore, M. D., Clarke, S., Redifer, M. E., Christie, R. J., Stoll, A. M., Dubois, A., Bevirt, J., Gibson, A. R., Foster, T. J., and Osterkamp, P. G., "Design and Performance of the NASA SCEPTOR Distributed Electric Propulsion Flight Demonstrator," *16th AIAA Aviation Technology, Integration, and Operations Conference*, AIAA Paper 2016-3920, June 2016. doi:10.2514/6.2016-3920.

[7] MacCready, P. B., "Regenerative Battery-Augmented Soaring," *Technical Soaring*, Vol. 23, No. 1, 1999, pp. 28–32.

[8] Galvão, F. L., "A Note on Glider Electric Propulsion," *Technical Soaring*, Vol. 36, No. 4, 2012, pp. 94–101.

[9] Barnes, J. P., "Flight Without Fuel – Regenerative Soaring Feasibility," *General Aviation Technology Conference and Exhibition*, SAE Technical Paper 2006-01-2422, Aug. 2006. doi:10.4271/2006-01-2422.

[10] Barnes, J. P., "Regenerative Electric Flight: Synergy and Integration of Dual-Role Machines," *53rd AIAA Aerospace Sciences Meeting*, AIAA Paper 2015-1302, Jan. 2015. doi:10.2514/6.2015-1302.

[11] Gunnarsson, G., Skúlason, J. B., Sigurbjarnarson, A., and Enge, S., "Regenerative Electric/Hybrid Drive Train for Ships," Nordic Innovation Publication 2016:02, Jan. 2016.

[12] Eržen, D., Andrejašič, M., Lapuh, R., Tomažič, J., Gorup, Č., and Kosel, T., "An Optimal Propeller Design for In-Flight Power Recuperation on an Electric Aircraft," *2018 Aviation Technology, Integration, and Operations Conference*, AIAA Paper 2018-3206, June 2018. doi:10.2514/6.2018-3206.

[13] Cherubini, A., Papini, A., Vertechy, R., and Fontana, M., "Airborne Wind Energy Systems: A review of the technologies," *Renewable and Sustainable Energy Reviews*, Vol. 51, 2015, pp. 1461 – 1476. doi:10.1016/j.rser.2015.07.053.

[14] Gill, A., Von Backström, T. W., and Harms, T. M., "Flow Fields in an Axial Flow Compressor During Four-Quadrant Operation," *Journal of Turbomachinery*, Vol. 136, No. 6, 2014. doi:10.1115/1.4025594.

[15] Ortolan, A., Courty-Audren, S.-K., Binder, N., Carbonneau, X., García Rosa, N., and Challas, F., "Experimental and Numerical Flow Analysis of Low-Speed Fans at Highly Loaded Windmilling Conditions," *Journal of Turbomachinery*, Vol. 139, No. 7, 2017. doi:10.1115/1.4035656.

[16] Binder, N., Courty-Audren, S.-K., Duplaa, S., Dufour, G., and Carbonneau, X., "Theoretical Analysis of the Aerodynamics of Low-Speed Fans in Free and Load-Controlled Windmilling Operation," *Journal of Turbomachinery*, Vol. 137, No. 10, 2015. doi:10.1115/1.4030308.

[17] Sinnige, T., de Vries, R., Della Corte, B., Avallone, F., Ragni, D., Eitelberg, G., and Veldhuis, L. L. M., "Unsteady Pylon Loading Caused by Propeller-Slipstream Impingement for Tip-Mounted Propellers," *Journal of Aircraft*, Vol. 55, No. 4, 2018, pp. 1605–1618. doi:10.2514/1.C034696.

[18] Stokkermans, T. C. A., van Arnhem, N., Sinnige, T., and Veldhuis, L. L. M., "Validation and Comparison of RANS Propeller Modeling Methods for Tip-Mounted Applications," *AIAA Journal*, Vol. 57, No. 2, 2019, pp. 566–580. doi:10.2514/1.J057398.

[19] Anon., "ANSYS® Academic Research Release 16.0 Help System, Fluent," ANSYS, inc., Canonsburg, PA, 2015.

[20] Barth, T. J., and Jespersen, D. C., "The Design and Application of Upwind Schemes on Unstructured Meshes," *27th Aerospace Sciences Meeting*, AIAA Paper 1989-366, Jan. 1989. doi:10.2514/6.1989-366.

© 2019 by T. Sinnige, T. C. A. Stokkermans, N. van Arnhem, and L. L. M. Veldhuis.
https://doi.org/10.2514/6.2019-3033

[21] Spalart, P. R., and Allmaras, S. R., "A One-Equation Turbulence Model for Aerodynamic Flows," *30th Aerospace Sciences Meeting*, AIAA Paper 1992-439, June 1992. doi:10.2514/6.1992-439.

[22] Dacles-Mariani, J., Zilliac, G. G., Chow, J. S., and Bradshaw, P., "Numerical/Experimental Study of a Wingtip Vortex in the Near Field," *AIAA Journal*, Vol. 33, No. 9, 1995, pp. 1561–1568. doi:10.2514/1.12826.

[23] Spalart, P. R., and Rumsey, C. L., "Effective Inflow Conditions for Turbulence Models in Aerodynamic Calculations," *AIAA Journal*, Vol. 45, No. 10, 2007, pp. 2544–2553. doi:10.2514/1.29373.

[24] Drela, M., and Youngren, M. H., "XROTOR Download Page," online, 2011. URL `http://web.mit.edu/drela/Public/web/xrotor/`, retrieved 1 August 2018.

[25] Drela, M., "XFOIL: An Analysis and Design System for Low Reynolds Number Airfoils," *Low Reynolds Number Aerodynamics*, edited by T. J. Mueller, Springer Berlin Heidelberg, Berlin, Heidelberg, 1989, pp. 1–12.

[26] Wood, D., "Small Wind Turbines," *Advances in Wind Energy Conversion Technology*, edited by M. Sathyajith and G. S. Philip, Springer Berlin Heidelberg, Berlin, Heidelberg, 2011, pp. 195–211. doi:10.1007/978-3-540-88258-9_8.

[27] van Arnhem, N., Sinnige, T., Stokkermans, T. C. A., Eitelberg, G., and Veldhuis, L. L. M., "Aerodynamic Interaction Effects of Tip-Mounted Propellers Installed on the Horizontal Tailplane," *2018 AIAA Aerospace Sciences Meeting*, AIAA Paper 2018-2052, Jan. 2018. doi:10.2514/6.2018-2052.